Space Sci Rev (2009) 144: 383–399
DOI 10.1007/s11214-008-9434-0

Coronal Holes and Open Magnetic Flux

Y.-M. Wang

Received: 1 July 2008 / Accepted: 28 August 2008 / Published online: 23 September 2008

Abstract Coronal holes are low-density regions of the corona which appear dark in X-rays and which contain "open" magnetic flux, along which plasma escapes into the heliosphere. Like the rest of the Sun's large-scale field, the open flux originates in active regions but is subsequently redistributed over the solar surface by transport processes, eventually forming the polar coronal holes. The total open flux and radial interplanetary field component vary roughly as the Sun's total dipole strength, which tends to peak a few years after sunspot maximum. An inverse correlation exists between the rate of flux-tube expansion in coronal holes and the solar wind speed at 1 AU. In the rapidly diverging fields present at the polar hole boundaries and near active regions, the bulk of the heating occurs at low heights, leading to an increase in the mass flux density at the Sun and a decrease in the asymptotic wind speed. The quasi-rigid rotation of coronal holes is maintained by continual footpoint exchanges between open and closed field lines, with the reconnection taking place at the streamer cusps. At much lower heights within the hole interiors, "interchange reconnection" between small bipoles and the overlying open flux also gives rise to coronal jets and polar plumes.

Keywords Coronal holes · Open magnetic flux · Solar wind · Photospheric flux transport · Coronal flux-tube expansion · Rigid rotation · Magnetic reconnection

1 Basic Concepts

Coronal holes are predominantly unipolar areas of the Sun where the magnetic field extends outward to form the interplanetary magnetic field (IMF) and plasma escapes to form the solar wind (see Zirker 1977; Cranmer 2002; McComas et al. 2007; Zurbuchen 2007). The approximate locations of these low-density coronal regions can be determined from the observed photospheric field by means of a potential-field source-surface (PFSS) extrapolation. In this empirically well-tested model, the corona is assumed to remain current-free

Y.-M. Wang (✉)
Code 7672W, Space Science Division, Naval Research Laboratory, Washington, DC 20375-5352, USA
e-mail: ywang@yucca.nrl.navy.mil

out to a spherical "source surface" at heliocentric distance $r = R_{ss} \sim 2.5\ R_\odot$, where the tangential field components are set to zero, mimicking the magnetohydrodynamic effect of the plasma pressure as it overcomes the restraining magnetic tension (Schatten et al. 1969). All field lines that cross this surface are considered to be open. At the inner boundary, the radial component of the potential field is matched to the photospheric field, which is taken to be radially oriented at the depth where it is measured. [Note that it is incorrect to match the line-of-sight components directly to each other, as done by Altschuler and Newkirk (1969), because the photospheric field, unlike the coronal field, is highly nonpotential.] That this simple prescription is able to reproduce the global configuration of X-ray and He I 1083.0 nm coronal holes at all phases of the sunspot cycle (Levine 1982; Wang et al. 1996; Neugebauer et al. 1998; Luhmann et al. 2002; Schrijver and DeRosa 2003) has important physical implications:

(1) Because higher order multipoles fall off rapidly with height, the main contribution to the source surface field and the open flux comes from the $l = 1$ and $l = 2$ (i.e., the dipole and, at sunspot maximum, the quadrupole) components of the photospheric field.
(2) Being composed of low-order multipoles, the coronal field (including coronal holes) must rotate more rigidly than the photospheric field, which is dominated by high-order multipoles.
(3) That the observed coronal-hole areas can be reproduced with R_{ss} fixed at $\sim 2.5\ R_\odot$ throughout the solar cycle implies that the plasma pressure p, and hence the coronal heating rate, must be a function of the magnetic field strength B. If the heating were instead described by a simple adiabatic law $p \propto \rho^\gamma$ (where ρ is the plasma density and γ the ratio of specific heats), the point where $p \sim B^2/8\pi$ would move outward and the polar holes would contract as the Sun's dipole strength increases, contrary to observations.

The PFSS model breaks down beyond $r \sim 2.5\ R_\odot$ because it omits the effect of transverse pressure gradients (Suess and Nerney 1975). The induced heliospheric sheet currents act to redistribute the open flux until it becomes independent of heliographic latitude L and longitude ϕ (Schatten 1971), in agreement with *Ulysses* magnetometer measurements (Balogh et al. 1995; Smith et al. 2001). To derive the radial IMF strength, we simply divide the total open flux Φ_{open} by $4\pi r^2$, where Φ_{open} is obtained by integrating $|B_r|$ over the source surface (Wang and Sheeley 1995; Lockwood et al. 1999). Thus, at $r = r_E = 1$ AU,

$$B_E = \frac{\Phi_{open}}{4\pi r_E^2}. \tag{1}$$

Because coronal holes occupy only a small fraction of the solar surface, the open flux initially tends to diverge very superradially, even when averaged over a supergranular area. The factor by which a given coronal flux tube expands in solid angle between its footpoint (taken to be just above the chromospheric canopy) and the source surface is given by

$$f_{ss} = \left(\frac{R_\odot}{R_{ss}}\right)^2 \frac{B_0}{B_{ss}}, \tag{2}$$

where B_0 and B_{ss} denote the field strengths at $r \simeq R_\odot$ and $r = 2.5\ R_\odot$, respectively. Empirically, it is found that the solar wind speed at 1 AU is inversely correlated with f_{ss} (Levine et al. 1977; Wang and Sheeley 1990a; Arge and Pizzo 2000): the more slowly the flux tube diverges in the corona, the higher the final wind speed [contrary to what is sometimes inferred from studies such as those of Munro and Jackson (1977) and Kopp and Holzer (1976)]. The

expansion factor is *relatively* small (but greater than unity) near the centers of large coronal holes, but diverges rapidly near the boundaries between opposite-polarity holes, where $B_{ss} \rightarrow 0$. It should be emphasized that, because the field lines do not actually become radial until $r \sim 5$–$10\ R_\odot$, f_{ss} does not represent the net expansion undergone by a flux tube between the Sun and 1 AU (which shows a quite different behavior), but only the expansion out to $r \sim 2.5\ R_\odot$.

2 Solar Cycle Variation of the Open Flux

We now derive some general properties of open field regions over the solar cycle by applying the PFSS model to the photospheric field, in the form of 27.3 day synoptic maps from the Mount Wilson Observatory (MWO) and the Wilcox Solar Observatory (WSO). To correct for the saturation of the Fe I 525.0 nm line profile, we have multiplied the magnetograph measurements by the latitude-dependent factor $(4.5 - 2.5 \sin^2 L)$ (Wang and Sheeley 1995; Ulrich et al. 2002; Arge et al. 2002).

Figure 1 compares the evolution of the total open flux during 1967–2008 with spacecraft measurements of the radial IMF strength at Earth. The two curves are in rough agreement, both varying by a factor of order 2 during each of the last three sunspot cycles. The open flux and IMF strength tend to peak ∼2–3 yr after sunspot maximum, when the Sun's total dipole strength is greatest. Also noteworthy is the weakness of the field during 2007–2008 (∼1.5 nT) compared to its average level during previous sunspot minima (∼2 nT).

As shown in Fig. 2(a), the total area occupied by open flux decreases from ∼20% of the solar surface near sunspot minimum to only ∼5% at sunspot maximum; at the same time, however, the average footpoint field strength in coronal holes increases from ∼5 G at

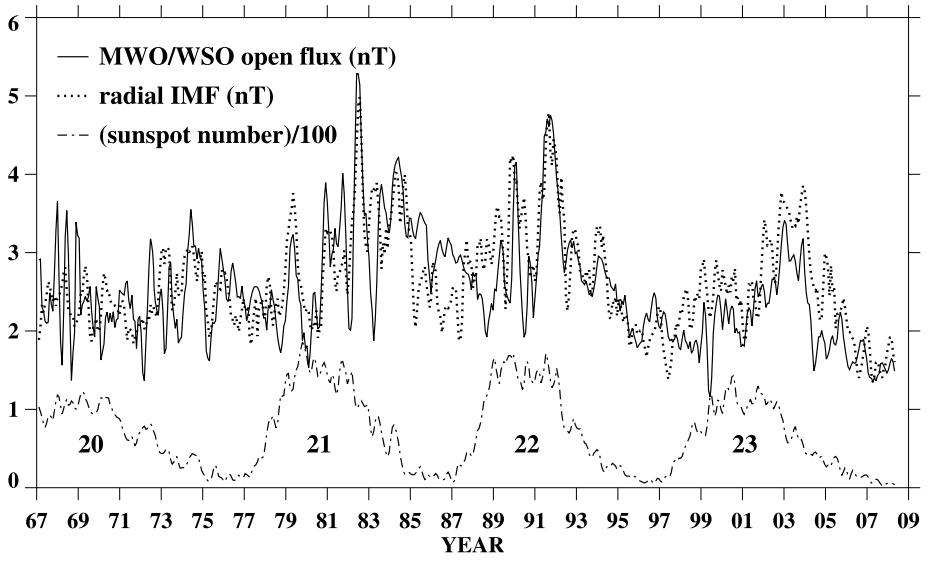

Fig. 1 Comparison between the near-Earth radial IMF strength (NSSDC OMNI 2 data) and the total open flux Φ_{open}, derived from a PFSS extrapolation of MWO and WSO magnetograph measurements and expressed as an equivalent field strength (nT) at 1 AU. Also plotted is the sunspot number. Here and in Fig. 2, three-month running means have been taken

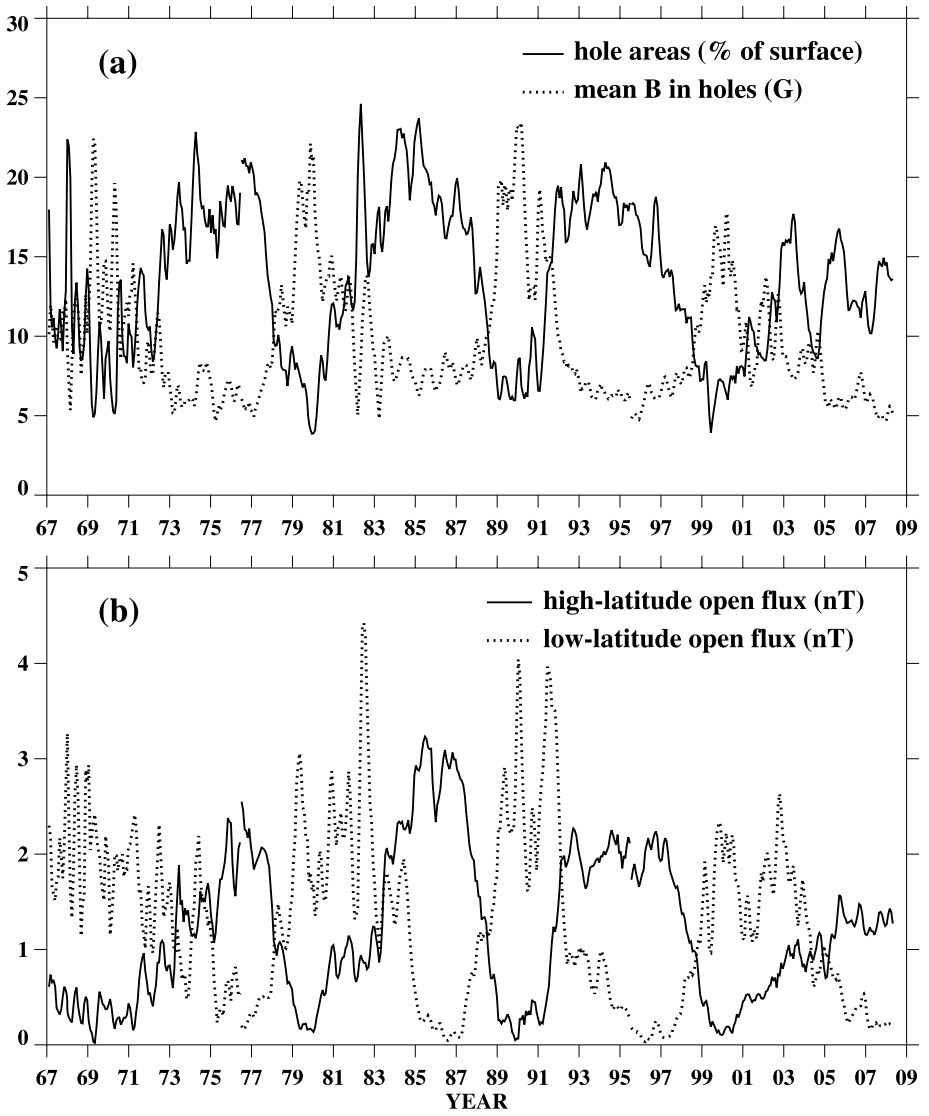

Fig. 2 (**a**) Time variation of the total surface area occupied by open flux (% of the solar surface) and of the average footpoint field strength in open regions (G). (**b**) Time variation of the open flux originating from high latitudes ($|L| > 45°$) and from low latitudes ($|L| < 45°$), expressed as field strengths (nT) at 1 AU

sunspot minimum to ∼20 G at sunspot maximum. The total open flux, which is the product of these two quantities, thus remains constant to within a factor of 2. From Fig. 2(b), we see that most of the open flux resides at high latitudes near sunspot minimum but at low latitudes near sunspot maximum. The low-latitude open flux is characterized by large footpoint field strengths because it is rooted in and around active regions. The high-latitude open flux is seen to be much weaker during the present activity minimum than during the 1976, 1986, and 1996 minima, reflecting the unusually weak polar fields at the end of cycle 23.

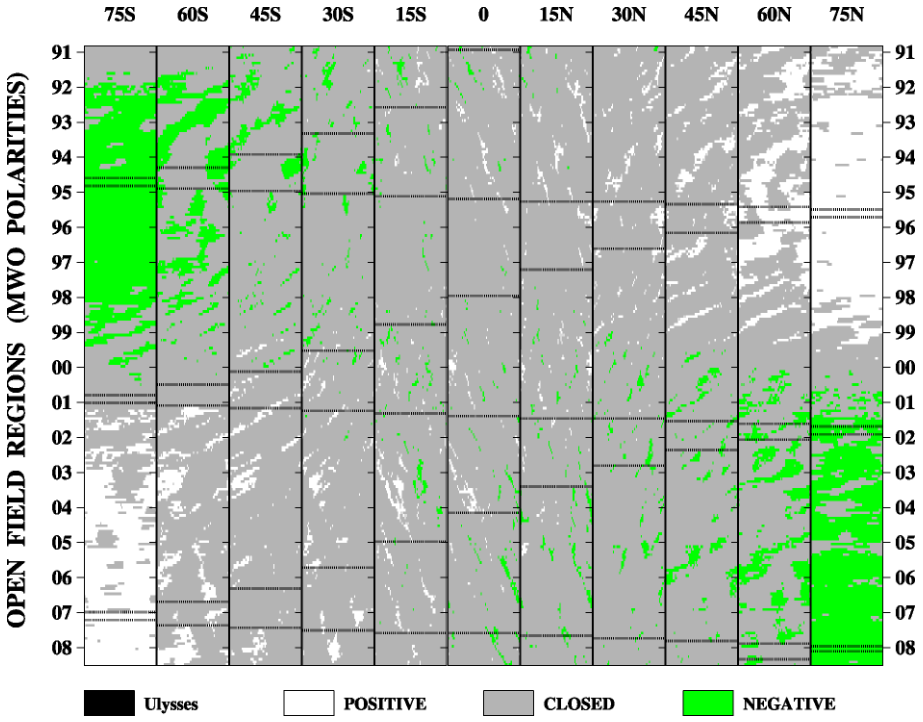

Fig. 3 Stackplot array showing the latitude-by-latitude evolution of coronal holes during 1990–2008. These footpoint areas of open flux were determined from a PFSS extrapolation of MWO magnetograph measurements. In each latitude panel, successive rows of pixels represent successive 27.3 day Carrington rotations, with longitude increasing from 0° at the left to 360° at the right. *White*: outward-pointing open flux. *Green*: inward-pointing open flux. *Gray*: closed field regions. *Horizontal lines*: latitude trajectory of *Ulysses*

The anticorrelation between coronal hole area and field strength suggested by Fig. 2(a) is mainly a consequence of photospheric flux transport (Sect. 3): the open flux is initially concentrated near the edges of active regions, but occupies a progressively larger area and decreases in strength as it diffuses over the solar surface.

The stackplot array in Fig. 3 shows, at a series of latitudes between $L = -75°$ and $L = +75°$, the evolution of open field regions during 1990–2008. In each latitude panel, successive rows of pixels represent successive Carrington rotations, with longitude ϕ increasing from left to right and time running in the opposite direction. The global picture is dominated by the waxing and waning of the polar holes, which disappear when the polar fields reverse near sunspot maximum. At lower latitudes, the coronal holes of a given polarity tend to form coherent patterns lasting up to ∼1–2 yr, with the patterns slanting downward and to the right (left) if they rotate faster (slower) than the 27.3 day Carrington rate.

That the polar holes are confined to latitudes above 60° is significant: it implies that the polar fields have a highly concentrated distribution near sunspot minimum, varying with latitude roughly as $\sin^7 L$ (Svalgaard et al. 1978; Wang and Sheeley 1995). If the polar fields instead had a simple dipole ($\sin L$) distribution, the polar hole boundaries would extend all the way down to latitude 40°. The bunched "topknot" form of the polar fields is also evident from observations of polar plumes, which are much more steeply inclined toward the equator than expected for a dipole field (Saito 1965). The extreme poleward concentration of the photospheric flux is due to the presence of the surface meridional flow.

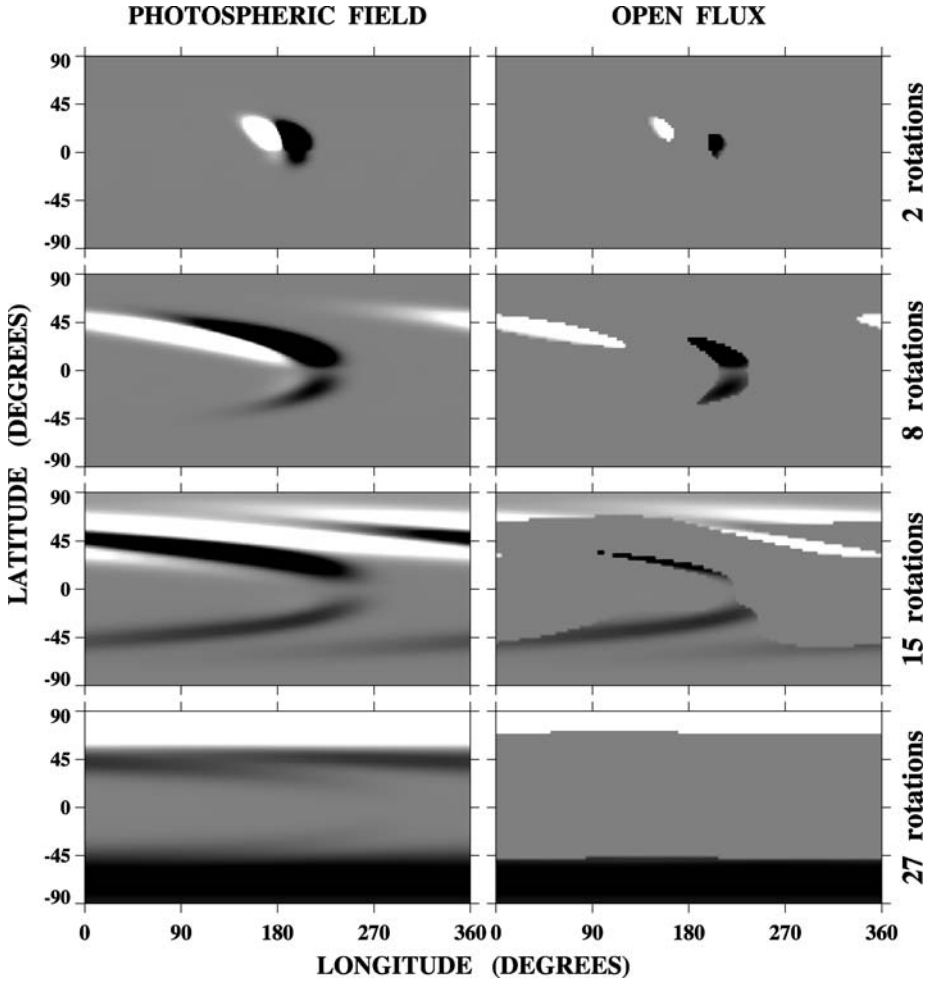

Fig. 4 Large BMR and associated open flux evolving under the influence of differential rotation, diffusion, and poleward flow. The bipole was deposited at latitude $L = +10°$ with a longitudinal (latitudinal) pole separation of 20° (4°). The Carrington-format maps display the distribution of the photospheric field (*left panels*) and of the open flux (*right panels*) after 2, 8, 15, and 27 rotations. *White* (*black*) denotes $B_r > 0$ ($B_r < 0$)

3 Flux Transport and the Formation of the Polar Coronal Holes

The relation between coronal holes and sunspot activity can be understood using a transport model for the photospheric field. We start with a single bipolar magnetic region (BMR) and allow it to evolve under the influence of the photospheric differential rotation, supergranular convection (turbulent diffusion) at a rate of 600 $\mathrm{km^2\,s^{-1}}$, and a poleward bulk flow of amplitude $V_\mathrm{m} = 15\ \mathrm{m\,s^{-1}}$. The BMR, representing a large, idealized active region, is deposited at latitude $L = +10°$, with its poles separated by 20° in longitude and 4° in latitude. The left panels in Fig. 4 show the distribution of the photospheric field after 2, 8, 15, and 27 (27.3 day) rotations, while the corresponding PFSS-derived open field regions are displayed at the right. A pair of small, opposite-polarity holes forms at time $t = 0$ at the far

corners of the BMR: these are the footpoint areas of the high loops that reach the source surface. The nonaxisymmetric (ϕ-dependent) component of the photospheric flux distribution $B_r(R_\odot, L, \phi, t)$ is sheared by the differential rotation, and diffusively annihilated as the latitudinal gradient $|\partial B_r/\partial L|$ progressively steepens. The meridional flow accelerates this process by carrying the BMR flux to midlatitudes, where the rotational gradients are largest. At the same time, a small amount of leading-polarity flux diffuses across the equator. After a time $\tau_{\rm flow} \sim R_\odot/V_{\rm m} \sim 1.5$ yr, the nonaxisymmetric component of the field (including the equatorial dipole moment) has decayed away and the remaining axisymmetric flux has been transported to the poles, forming the polar fields with their embedded holes. Note that the axis of the BMR must be tilted with respect to the east-west line in order for any net flux to reach the poles. Also, it is evident that our newly created polar fields could be canceled again by depositing another BMR with reversed east-west polarity orientation and continuing the simulation.

As remarked in relation to the stackplots of Fig. 3, low-latitude coronal holes and the equatorward extensions of the polar holes tend to form coherent patterns lasting ~1–2 yr. Likewise, an inspection of Figs. 1 and 2 suggests that the peaks in the radial IMF strength and in the low-latitude open flux are typically on the order of a year wide. This characteristic width corresponds to the decay time for the equatorial dipole field, which in turn is determined by $\tau_{\rm flow}$, the timescale for the surface meridional flow to carry the active region fields to midlatitudes. The same process may be responsible for some of the ~1.2–1.7 yr quasi-periodicities detected intermittently in the IMF, solar wind, and geomagnetic activity (Silverman and Shapiro 1983; Richardson et al. 1994; Mursula et al. 2003).

4 Solar Wind Speed, Coronal Heating, and Flux-Tube Expansion

Figure 5 compares the proton flow speeds recorded at *Ulysses* during 1990–2008 with the flux-tube expansion factors $f_{\rm ss}$ derived from MWO photospheric field measurements. We conclude from the similar appearance of the two stackplots that fast wind is associated with relatively small expansion factors, and slow wind with very large expansion factors. The three main bands of very fast wind (low expansion) correspond to the *Ulysses* polar passes of 1994–1995, 2001–2002, and 2006–2008.

Now using $f_{\rm ss}$ as an (inverse) proxy for wind speed, we display in Fig. 6 the global patterns of wind speed during 1990–2008 (compare Fig. 3, which shows the underlying distribution of coronal holes). The global picture is dominated by the high-speed wind from the polar holes, whose large interiors are characterized by relatively slow flux-tube expansion. As the polar holes recede and disappear at sunspot maximum, low-speed wind spreads from low latitudes all the way to the poles. The sources of this wind are the many small holes located around active regions and containing strong, rapidly diverging fields (Levine 1982; Wang and Sheeley 1990b; Kojima et al. 1999; Neugebauer et al. 2002; Schrijver and DeRosa 2003; Liewer et al. 2004; Sakao et al. 2007). In contrast, the bulk of the low-speed wind near sunspot minimum comes from the rapidly diverging flux tubes at the polar hole boundaries.

The physical basis for the wind speed–expansion factor relationship can be understood as follows. Let us assume the existence of a heating source in coronal holes which varies with radial distance. If the bulk of the energy is deposited close to the coronal base, the downward heat conduction will act to drive a large mass flux, and the energy available per solar wind proton will be reduced. In contrast, if the energy is deposited over a larger distance extending toward the sonic point, more of it will go into accelerating the wind and

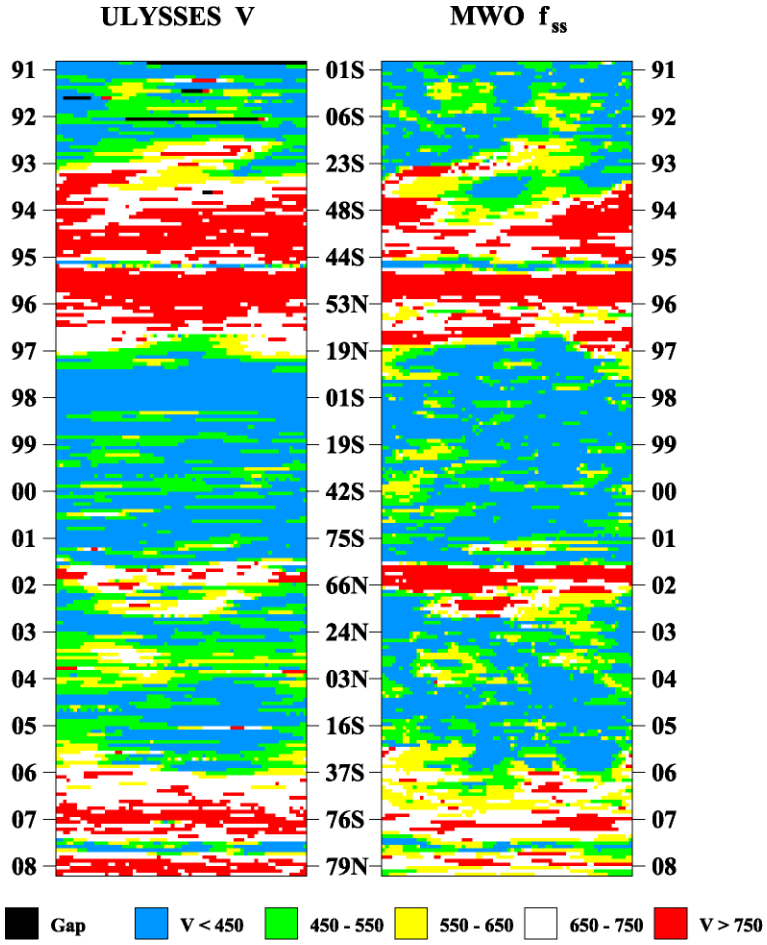

Fig. 5 Stackplots comparing the daily wind speeds V observed at *Ulysses* during 1990–2008 (*left*) with the values predicted by applying the expansion factor model to MWO photospheric field measurements (*right*). Carrington longitude runs from left to right; the heliographic latitude and heliocentric distance (in AU) of the spacecraft are given alongside the horizontal ticks marking the start of each year. *Red*: $V > 750$ km s^{-1} ($f_{ss} < 4.5$). *White*: $V = 650$–750 km s^{-1} ($4.5 < f_{ss} < 7$). *Yellow*: $V = 550$–650 km s^{-1} ($7 < f_{ss} < 10$). *Green*: $V = 450$–550 km s^{-1} ($10 < f_{ss} < 20$). *Blue*: $V < 450$ km s^{-1} ($f_{ss} > 20$). *Black*: data gap

less into increasing the mass flux (Leer and Holzer 1980). If the source of the heating is the coronal magnetic field, we would then expect a rapidly diverging field to be characterized by a shorter damping length and produce slower wind than a more gradually diverging field.

We illustrate these points by numerically solving the single-fluid equations of mass, momentum, and energy conservation for a thermally driven wind, including the effects of coronal heating, heat conduction, and radiative losses (*cf.* Hammer 1982; Withbroe 1988). The flow is taken to be along a radially oriented flux tube, with the magnetic field $B(r)$ falling off as $r^{-\nu}$ for $r \lesssim 2.5\ R_\odot$ and as r^{-2} for $r \gg 2.5\ R_\odot$. The model explicitly includes a chromospheric-coronal transition region, where the downward heat flux is balanced by radiation and an outward enthalpy flux (which in turn determines the mass flux). To demonstrate that a coronal heating rate that depends mainly on the local magnetic field strength will lead

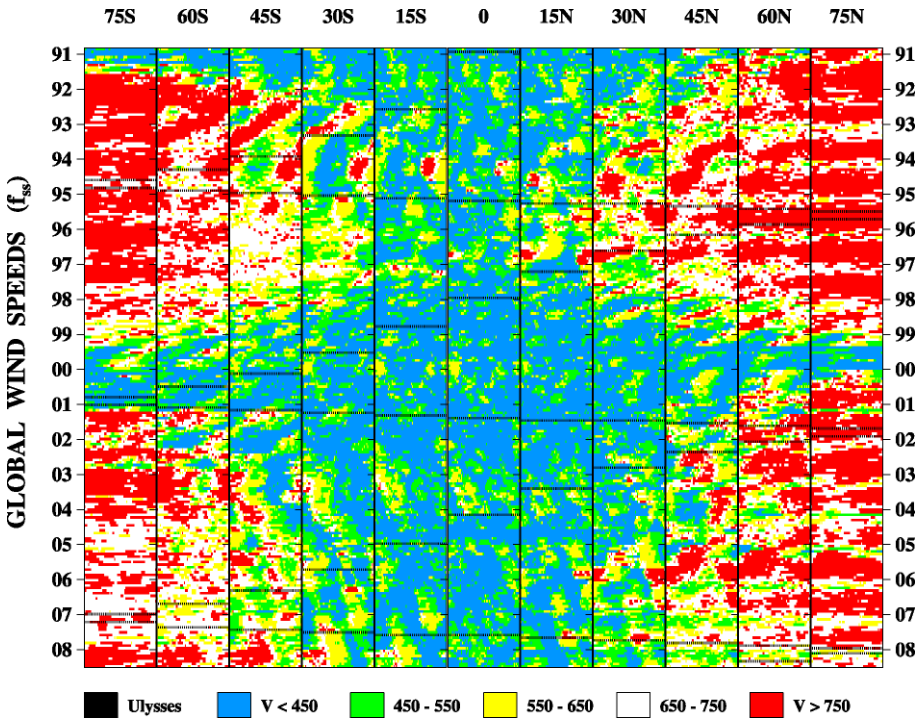

Fig. 6 Multilatitude stackplot array showing the global evolution of the solar wind speed during 1990–2008, as derived from the expansion factor relationship. In each latitude panel, successive rows of pixels represent successive 27.3 day Carrington rotations, with longitude increasing from left to right. Color-coding as in Fig. 5. *Black horizontal lines* indicate the latitude trajectory of *Ulysses*

to an inverse relationship between wind speed and expansion factor, we arbitrarily adopt a heating function of the form

$$F_{\rm h} = F_{\rm h0} \left(\frac{B}{B_0} \right)^{\mu}, \tag{3}$$

where, for definiteness, we take $F_{\rm h0} = 8 \times 10^5$ erg cm^{-2} s^{-1} and $\mu = 3/2$. Figure 7 shows the steady-state profiles of flow speed $u(r)$, temperature $T(r)$, proton (or electron) density $n(r)$, and proton flux $n(r)u(r)$ obtained by setting ν equal to 2, 3, and 4. As the magnetic falloff rate increases, the location of the temperature maximum moves inward, the mass flux density at the coronal base increases, the temperatures fall in the outer corona, and the flow velocity at the outer boundary decreases. Similar results hold for any $\mu > 1$.

A possible source of the heating in coronal holes is reconnection between the unipolar flux concentrations and the ubiquitous "magnetic carpet," consisting of small bipoles that continually emerge at the photosphere; this network and intranetwork activity may in turn give rise to MHD waves that propagate outward into the corona before eventually dissipating (see, e.g., Parker 1991; Schrijver et al. 1998). According to Cranmer et al. (2007), however, incompressible Alfvén waves are generated by granular motions and subsequently damped via a turbulent cascade. Since the volumetric heating rate varies as $L_\perp^{-1} \propto B^{1/2}$, where $L_\perp$ is the transverse correlation length for the turbulence (*cf.* Hollweg 1986), Cranmer et al. likewise find that the wind speed is inversely correlated with the rate of magnetic falloff.

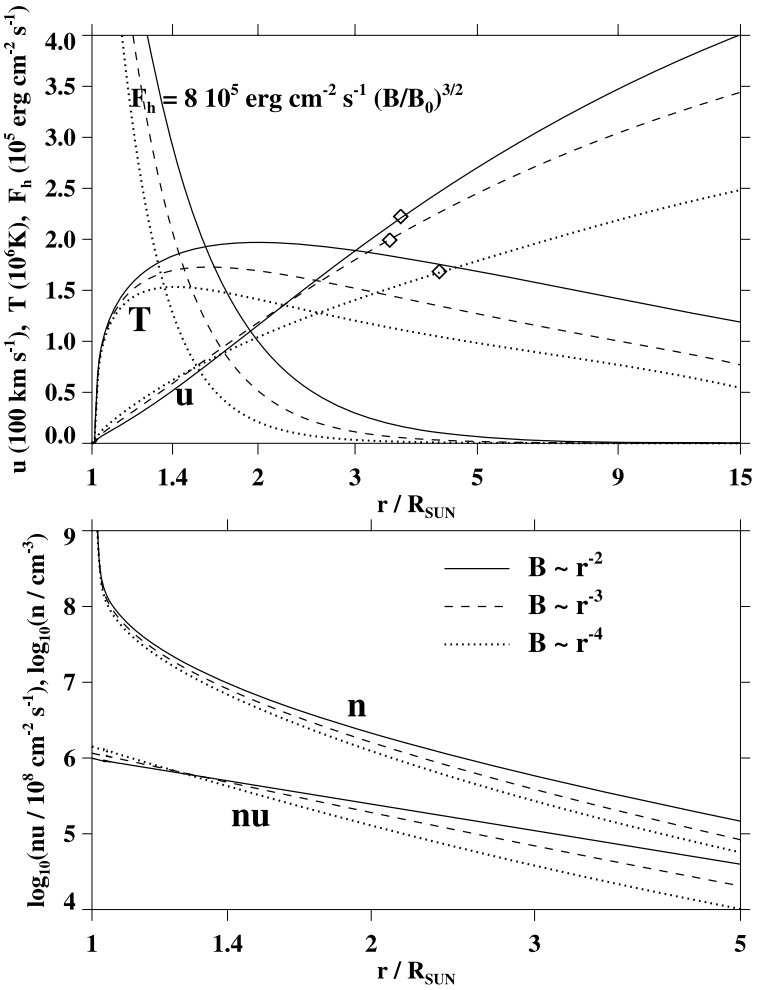

Fig. 7 Three thermally driven wind solutions obtained by varying the magnetic falloff rate in the coronal heating function $F_{\rm h}(r) = 8 \times 10^5$ erg cm^{-2} s^{-1} $(B/B_0)^{3/2}$. *Solid lines*: $\nu = 2$. *Dashed lines*: $\nu = 3$. *Dotted lines*: $\nu = 4$. *Diamonds* mark the location of the sonic point

The relationship between network activity and coronal heating is especially clear in polar plumes. In this case, strong localized heating occurs near the base of the plume, where a small bipole (in the form of an EUV bright point) undergoes reconnection with a unipolar flux concentration inside the polar hole. This extra base heating drives a large downward heat flux and raises the density everywhere along the flux tube, while causing the temperature and flow speed above the dissipation region to *decrease* (Wang 1994), as confirmed by SUMER and UVCS observations (Wilhelm et al. 1998; Giordano et al. 2000; Teriaca et al. 2003). The plume decays after the minority-polarity flux is canceled on the ∼1 day timescale of the supergranular convection.

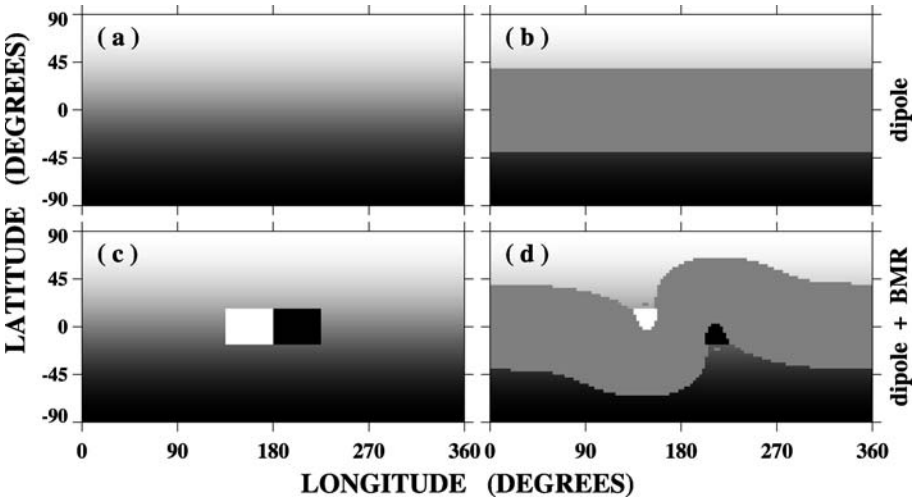

Fig. 8 Interaction between an equatorial BMR and the polar fields. (**a**) Axisymmetric dipole field of strength 1 G; (**b**) corresponding distribution of open flux (*gray* represents closed fields). (**c**) Superposition of a BMR of strength 5 G and an axisymmetric dipole of strength 1 G; (**d**) corresponding distribution of open flux. The flux distributions are all plotted at the solar surface

5 Magnetic Reconnection and the Rotation of Coronal Holes

The tendency for coronal holes to rotate more rigidly than the photosphere is most striking in the equatorward extensions of the polar holes (Timothy et al. 1975). This behavior becomes less puzzling once it is understood how these extensions are formed. Consider an idealized initial configuration consisting of an axisymmetric dipole field with its associated polar holes (Fig. 8, top panels). After depositing an east-west oriented BMR at the equator, we obtain a pair of equatorward extensions that link each polar hole to the like-polarity sector of the bipole (Fig. 8, bottom panels).

We now include the photospheric differential rotation, with angular velocity profile $\omega(L) = 13.38 - 2.30\sin^2 L - 1.62\sin^4 L$ deg day^{-1} (Snodgrass 1983), and allow the system to evolve with time. The leftmost panels in Fig. 9 show the photospheric field after 0, 1, and 2 (27.3 day) rotations, the middle panels show the corresponding open field regions, while the rightmost panels illustrate how the same regions would evolve if they sheared at the local plasma rate. We see that the PFSS-derived polar hole extensions hardly change their shape at all during the simulation. This result follows immediately from the fact that the large-scale photospheric flux distribution, which uniquely determines the coronal field in the current-free approximation, is practically time-independent in a frame that corotates with the BMR.

In reality, in the presence of a plasma, the coronal field must undergo continual reconnection in order to remain close to a potential state (see the MHD simulation of Lionello et al. 2005). Possible evidence for "interchange reconnection" between open and closed field lines is provided by coronagraph observations of density inhomogeneities that propagate outward along the heliospheric current/plasma sheet (Sheeley et al. 1997; Wang et al. 1998a; Crooker et al. 2004). The blobs appear to originate from the closed portions of helmet streamers and to be squeezed out through their cusps (Fig. 10). One interpretation of these white-light observations is that the streamer loops are undergoing reconnection with neighboring open field lines at the Y-point, leading to an exchange of footpoints in such a way

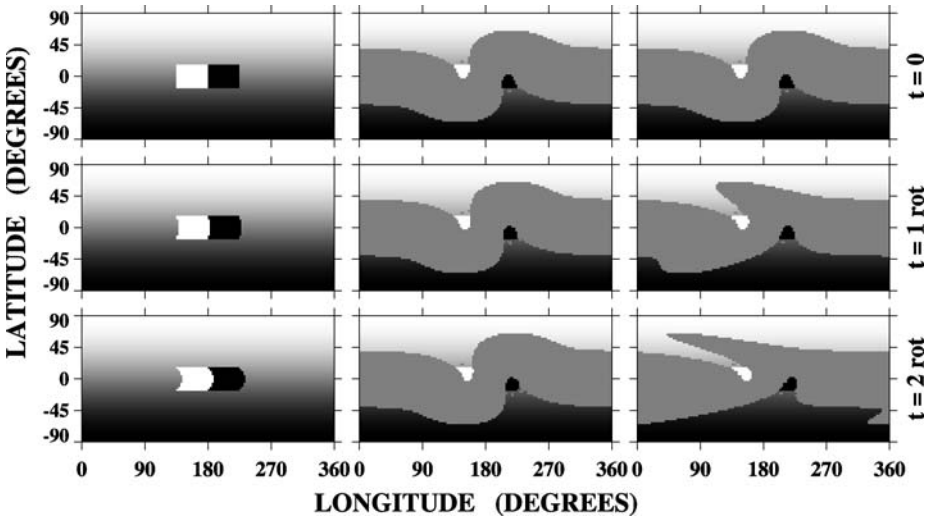

Fig. 9 Rotational evolution of a configuration consisting of a 5 G BMR at the equator and a 1 G axisymmetric dipole field. *Left*: Photospheric field after the lapse of 0, 1, and 2 rotations. *Middle*: Corresponding open field regions. *Right*: Open field regions as they would appear if they rotated at the photospheric plasma rate

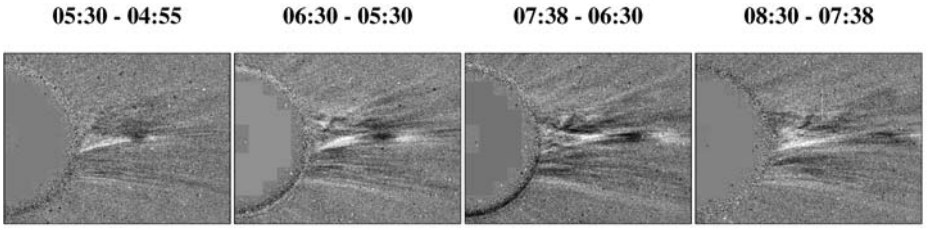

Fig. 10 Sequence of *SOHO* LASCO C2 running-difference images showing the ejection of a plasma blob from the cusp of a helmet streamer, 25 February 1997. The blob first appears as a slight density enhancement (*white* feature) near $r \sim 3.5\ R_{\odot}$. Note the background of fine raylike structures threading the plasma sheet, which may represent open field lines that have undergone interchange reconnection with the closed streamer loops

as to oppose the deformation (by rotational shearing or supergranular convective motions) of the coronal hole boundaries. At the same time, material is injected into the plasma sheet without eroding the helmet streamer or changing the total amount of open flux.

In addition to the outward-moving streamer blobs, the LASCO C2 coronagraph has detected thousands of inflow events at heliocentric distances of 2 to 5 $R_{\odot}$, again concentrated around the heliospheric current/plasma sheet (Sheeley and Wang 2002). A typical example is displayed in Fig. 11: the inward-moving structure leaves a narrow, dark trail in its wake; as it approaches the inner edge of the coronagraph field of view at $r \sim 2\ R_{\odot}$, it decelerates and takes on a cusp-like appearance. Such events, seen most frequently during times of high solar activity, are strongly suggestive of the closing-down of magnetic flux at coronal hole boundaries or (in some cases) in the aftermath of CMEs. The U-loops that result from the disconnection process should be detectable at 1 AU as disruptions in the suprathermal electron strahl streaming away from the Sun. While heat flux dropouts are common near the heliospheric current sheet, Crooker and Pagel (2008) conclude that they may signal either

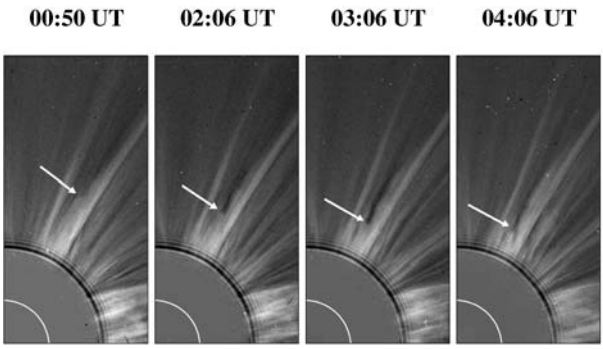

Fig. 11 Inflow observed with the LASCO C2 coronagraph on 25 October 1999. The sinking column of streamer material leaves a dark depletion trail in its wake and takes on a cusp-like appearance below $r \sim 2.5\ R_\odot$

disconnection or interchange reconnection (where one end of the field line remains anchored to the Sun).

6 Coronal Holes, Jets, and ^{3}He-Rich Particle Events

Coronal holes are copious emitters of X-ray and EUV jets (Shibata et al. 1992; Moses et al. 1997; Cirtain et al. 2007). The ejections are triggered by X-point reconnection between the small bipoles that continually emerge inside the holes and the overlying open flux, which acts to collimate the hot plasma and channel it out into the heliosphere (Shimojo and Shibata 2000). A single flaring bright point may emit several jets during its lifetime. The brighter and faster jets are also detected in white light beyond $r \sim 2\ R_\odot$, with their leading edges traveling at speeds of ~400–1000 km s^{-1} (Wang et al. 1998b).

The largest jets originate from small, flaring active regions located inside or near the boundaries of low-latitude coronal holes. In some cases, the source of the jets may be connected to Earth along the Parker spiral, allowing the energetic particles associated with these reconnection events to be observed *in situ*.

Figure 12 shows two EUV/white-light jet events originating from an active region near the west limb on 5 October 2002. The change in direction between the EUV jet and the corresponding white-light ejection above $r \sim 2\ R_\odot$ can be understood from the PFSS extrapolation in Fig. 13, which shows the southward-pointing open field lines adjacent to the flaring region bending sharply northward at greater heights. Over a 5-day interval beginning on October 3, the same small active region produced as many as 16 jet events, some of which consisted of multiple ejections (see Fig. 14). Early on October 5, the ULEIS detector on *ACE* recorded a steep increase in the flux of ^{3}He and Fe ions as connection to the source was established; the flux remained high over the next two days, and then fell on October 7 (Fig. 15). The highest peak in the particle intensity occurred ~8 hr after the event shown in the bottom panels of Fig. 12. Recent studies suggest that such impulsive solar energetic particle (SEP) events invariably originate from small active regions next to or inside coronal holes, whose open field lines channel the fractionated products of the reconnection process into the heliosphere (Reames 2002; Wang et al. 2006; Pick et al. 2006; Nitta et al. 2006).

7 Concluding Remarks

In this overview, we have emphasized the role of active regions, surface flux transport, and magnetic reconnection in the formation, evolution, and rotation of coronal holes. Much of

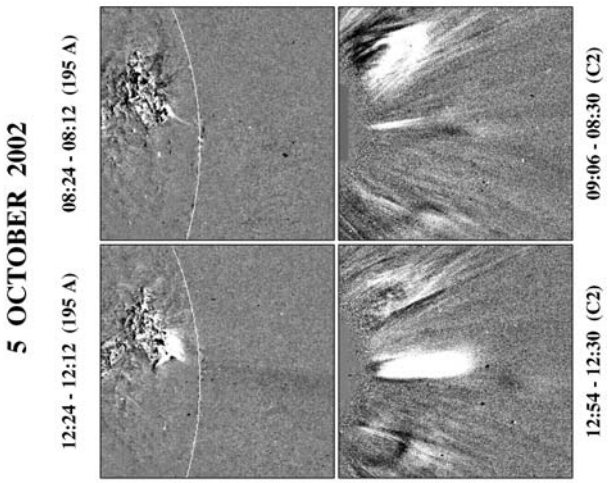

Fig. 12 Difference images showing two "homologous" *SOHO* LASCO/EIT jet events on 5 October 2002. The Fe XII 19.5 nm jets are on the *left*, while their white-light counterparts beyond $r \sim 2\ R_\odot$ are on the *right*. Note the change in direction of the jets as they propagate from the solar surface to the outer corona (compare Fig. 13)

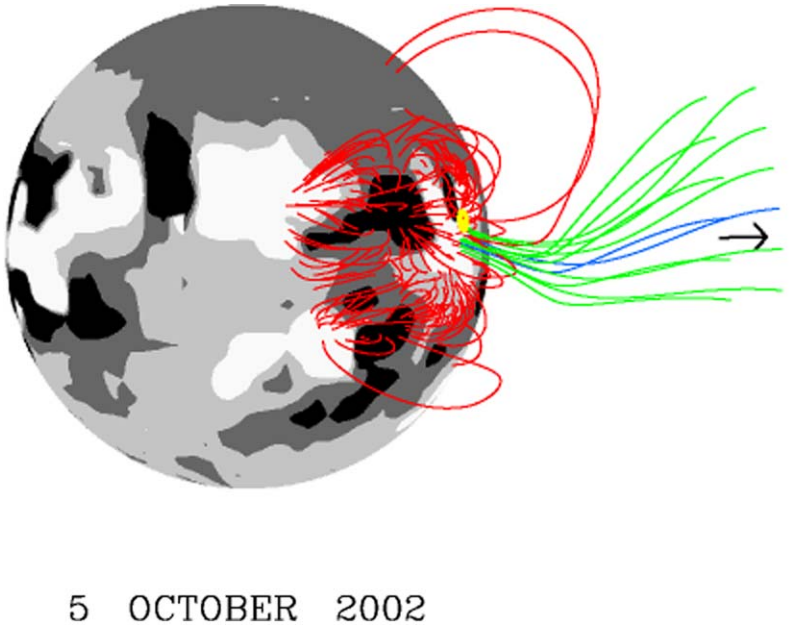

Fig. 13 Field-line configuration of the source region of the 5 October 2002 jets, derived by extrapolating the observed photospheric field. The open field lines (coded *blue* if directed into the ecliptic, *green* otherwise) point southward near the solar surface but bend northward at greater heights, thus accounting for the differing orientations of the EUV and white-light jets in Fig. 12. The *yellow dot* marks the location of the flaring source; the *arrow* indicates the direction of the LASCO C2 jets

this discussion has been based on approximating the coronal field as current-free. A major limitation of this approach is that it does not tell us how coronal loops open up to form long-lived coronal holes (are CME events involved, as suggested by Luhmann et al. 1998?), how the field-line reconnection that maintains their quasi-rigid rotation actually takes place, or how the open flux eventually closes down. These questions can addressed both observa-

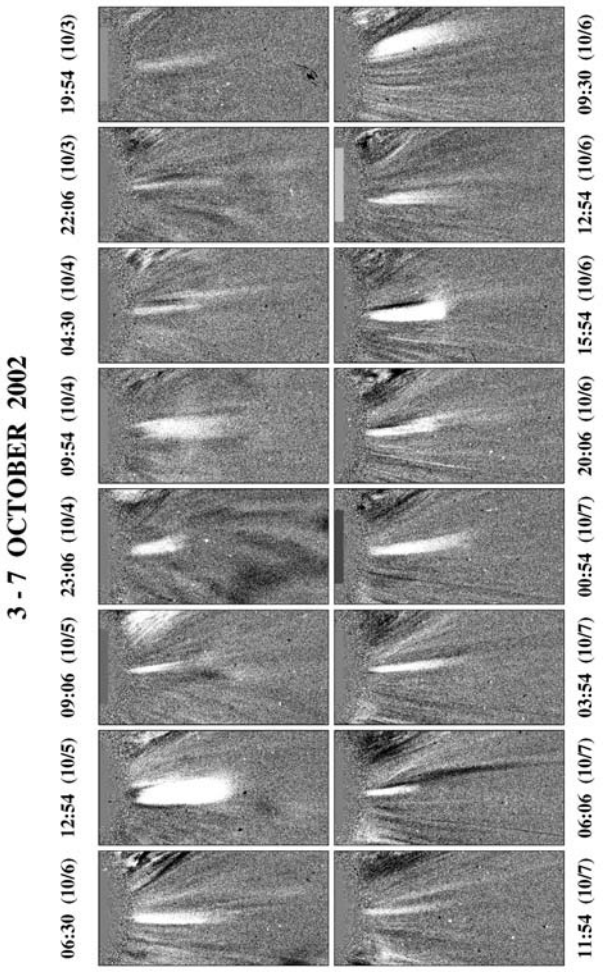

Fig. 14 The white-light jets shown in Fig. 12 were just two of 16 such events recorded by the LASCO C2 coronagraph from the same flaring active-region–coronal-hole system during 3–7 October 2002. The average speed of the jets was close to 700 km s^{-1}

tionally and with the help of 3D MHD simulations. In particular, the SECCHI white-light and EUV instruments on the twin *STEREO* spacecraft will make it easier to relate CMEs, slow streamer expansions/disruptions, streamer blobs, and inflow events (all of which are best observed near the sky plane) to changes in coronal hole boundaries (which are most visible on the disk).

Another unresolved issue concerns the sources of low-speed solar wind, which is characterized by high temporal and spatial variability and distinctive compositional properties (Bame et al. 1977; Geiss et al. 1995; von Steiger et al. 2000; Ko et al. 2006). It is often argued that this plasma must originate outside coronal holes, i.e., from closed field regions (Schwadron et al. 1999; Zurbuchen et al. 2000; Woo et al. 2004; Feldman et al. 2005; McComas et al. 2007; Zurbuchen 2007). We have suggested instead that the bulk of the slow wind comes either from just inside the boundaries of large coronal holes or from the small, rapidly evolving open field regions present around active regions. The high freeze-in temperatures (or $n_{O^{7+}}/n_{O^{6+}}$ ratios) measured in the slow wind and its tendency to be relatively enriched in elements of low first-ionization potential (FIP) are then attributed to the heating being concentrated near the coronal base, which steepens the local temperature gradient

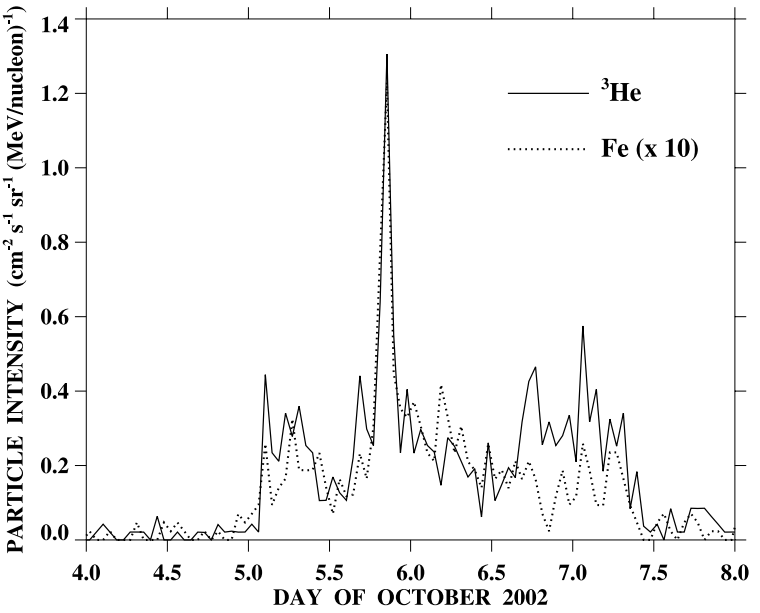

Fig. 15 Ion intensities in the 0.32–0.45 MeV nucleon^{-1} range measured by *ACE*/ULEIS during 4–7 October 2002 (compare Fig. 14). *Solid curve*: ^{3}He. *Dotted curve*: Fe. The highest peak occurs ∼8 hr after the flare/jet event displayed in the bottom panels of Fig. 12

and leads to enhanced chromospheric evaporation (Wang and Sheeley 2003). Self-consistent modeling of coronal heating and solar wind acceleration, along the lines of Cranmer et al. (2007) and Suzuki and Inutsuka (2006), may eventually help to settle this debate.

Acknowledgements I am indebted to N.R. Sheeley Jr. for his long-standing and continuing collaboration, to R. Grappin for developing the solar wind code used to obtain the results in Fig. 7, and to A. Balogh for inviting me to attend the ISSI Workshop "Origin and Dynamics of Solar Magnetism." Financial support was provided by NASA and the Office of Naval Research.

References

M.D. Altschuler, G. Newkirk Jr., Sol. Phys. **9**, 131 (1969)
C.N. Arge, V.J. Pizzo, J. Geophys. Res. **105**, 10465 (2000)
C.N. Arge, E. Hildner, V.J. Pizzo, J.W. Harvey, J. Geophys. Res. **107**, A10 (2002), SSH 16-1
A. Balogh, E.J. Smith, B.T. Tsurutani, D.J. Southwood, R.J. Forsyth, T.S. Horbury, Science **268**, 1007 (1995)
S.J. Bame, J.R. Asbridge, W.C. Feldman, J.T. Gosling, J. Geophys. Res. **82**, 1487 (1977)
J.W. Cirtain et al., Science **318**, 1580 (2007)
S.R. Cranmer, Space Sci. Rev. **101**, 229 (2002)
S.R. Cranmer, A.A. van Ballegooijen, R.J. Edgar, Astrophys. J. Suppl. Ser. **171**, 520 (2007)
N.U. Crooker, C. Pagel, J. Geophys. Res. **113**, A02106 (2008)
N.U. Crooker, C.-L. Huang, S.M. Lamassa, D.E. Larson, S.W. Kahler, H.E. Spence, J. Geophys. Res. **109**, A03107 (2004)
U. Feldman, E. Landi, N.A. Schwadron, J. Geophys. Res. **110**, A07109 (2005)
J. Geiss, G. Gloeckler, R. von Steiger, Space Sci. Rev. **72**, 49 (1995)
S. Giordano, E. Antonucci, G. Noci, M. Romoli, J.L. Kohl, Astrophys. J. **531**, L79 (2000)
R. Hammer, Astrophys. J. **259**, 767 (1982)
J.V. Hollweg, J. Geophys. Res. **91**, 4111 (1986)

Y.-K. Ko, J.C. Raymond, T.H. Zurbuchen, P. Riley, J.M. Raines, L. Strachan, Astrophys. J. **646**, 1275 (2006)
M. Kojima, K. Fujiki, T. Ohmi, M. Tokumaru, A. Yokobe, K. Hakamada, J. Geophys. Res. **104**, 16993 (1999)
R.A. Kopp, T.E. Holzer, Sol. Phys. **49**, 43 (1976)
E. Leer, T.E. Holzer, J. Geophys. Res. **85**, 4681 (1980)
R.H. Levine, Sol. Phys. **79**, 203 (1982)
R.H. Levine, M.D. Altschuler, J.W. Harvey, J. Geophys. Res. **82**, 1061 (1977)
P.C. Liewer, M. Neugebauer, T. Zurbuchen, Sol. Phys. **223**, 209 (2004)
R. Lionello, P. Riley, J.A. Linker, Z. Mikić, Astrophys. J. **625**, 463 (2005)
M. Lockwood, R. Stamper, M.N. Wild, Nature **399**, 437 (1999)
J.G. Luhmann, J.T. Gosling, J.T. Hoeksema, X. Zhao, J. Geophys. Res. **103**, 6585 (1998)
J.G. Luhmann, Y. Li, C.N. Arge, P.R. Gazis, R. Ulrich, J. Geophys. Res. **107**, A8 (2002), SMP 3-1
D.J. McComas et al., Rev. Geophys. **45**, RG1004 (2007)
D. Moses et al., Sol. Phys. **175**, 571 (1997)
R.H. Munro, B.V. Jackson, Astrophys. J. **213**, 874 (1977)
K. Mursula, B. Zieger, J.H. Vilppola, Sol. Phys. **212**, 201 (2003)
M. Neugebauer et al., J. Geophys. Res. **103**, 14587 (1998)
M. Neugebauer, P.C. Liewer, E.J. Smith, R.M. Skoug, T.H. Zurbuchen, J. Geophys. Res. **107**, A12 (2002), SSH 13-1
N.V. Nitta, D.V. Reames, M.L. DeRosa, Y. Liu, S. Yashiro, N. Gopalswamy, Astrophys. J. **650**, 438 (2006)
E.N. Parker, Astrophys. J. **372**, 719 (1991)
M. Pick, G.M. Mason, Y.-M. Wang, C. Tan, L. Wang, Astrophys. J. **648**, 1247 (2006)
D.V. Reames, Astrophys. J. **571**, L63 (2002)
J.D. Richardson, K.I. Paularena, J.W. Belcher, A.J. Lazarus, Geophys. Res. Lett. **21**, 1559 (1994)
K. Saito, Publ. Astron. Soc. Jpn. **17**, 1 (1965)
T. Sakao et al., Science **318**, 1585 (2007)
K.H. Schatten, Cosm. Electrodyn. **2**, 232 (1971)
K.H. Schatten, J.M. Wilcox, N.F. Ness, Sol. Phys. **6**, 442 (1969)
C.J. Schrijver, M.L. DeRosa, Sol. Phys. **212**, 165 (2003)
C.J. Schrijver et al., Nature **394**, 152 (1998)
N.A. Schwadron, L.A. Fisk, T.H. Zurbuchen, Astrophys. J. **521**, 859 (1999)
N.R. Sheeley Jr., Y.-M. Wang, Astrophys. J. **579**, 874 (2002)
N.R. Sheeley Jr. et al., Astrophys. J. **484**, 472 (1997)
K. Shibata et al., Publ. Astron. Soc. Jpn. **44**, L173 (1992)
M. Shimojo, K. Shibata, Astrophys. J. **542**, 1100 (2000)
S.M. Silverman, R. Shapiro, J. Geophys. Res. **88**, 6310 (1983)
E.J. Smith, A. Balogh, R.J. Forsyth, D.J. McComas, Geophys. Res. Lett. **28**, 4159 (2001)
H.B. Snodgrass, Astrophys. J. **270**, 288 (1983)
S.T. Suess, S.F. Nerney, Sol. Phys. **40**, 487 (1975)
T.K. Suzuki, S. Inutsuka, J. Geophys. Res. **111**, A06101 (2006)
L. Svalgaard, T.L. Duvall Jr., P.H. Scherrer, Sol. Phys. **58**, 225 (1978)
L. Teriaca, G. Poletto, M. Romoli, D.A. Biesecker, Astrophys. J. **588**, 566 (2003)
A.F. Timothy, A.S. Krieger, G.S. Vaiana, Sol. Phys. **42**, 135 (1975)
R.K. Ulrich, S. Evans, J.E. Boyden, L. Webster, Astrophys. J. Suppl. Ser. **139**, 259 (2002)
R. von Steiger et al., J. Geophys. Res. **105**, 27217 (2000)
Y.-M. Wang, Astrophys. J. **435**, L153 (1994)
Y.-M. Wang, N.R. Sheeley Jr., Astrophys. J. **355**, 726 (1990a)
Y.-M. Wang, N.R. Sheeley Jr., Astrophys. J. **365**, 372 (1990b)
Y.-M. Wang, N.R. Sheeley Jr., Astrophys. J. **447**, L143 (1995)
Y.-M. Wang, N.R. Sheeley Jr., Astrophys. J. **587**, 818 (2003)
Y.-M. Wang, S.H. Hawley, N.R. Sheeley Jr., Science **271**, 464 (1996)
Y.-M. Wang et al., Astrophys. J. **498**, L165 (1998a)
Y.-M. Wang et al., Astrophys. J. **508**, 899 (1998b)
Y.-M. Wang, M. Pick, G.M. Mason, Astrophys. J. **639**, 495 (2006)
K. Wilhelm, E. Marsch, B.N. Dwivedi, D.M. Hassler, P. Lemaire, A.H. Gabriel, M.C.E. Huber, Astrophys. J. **500**, 1023 (1998)
G.L. Withbroe, Astrophys. J. **325**, 442 (1988)
R. Woo, S.R. Habbal, U. Feldman, Astrophys. J. **612**, 1171 (2004)
J.B. Zirker (ed.), *Coronal Holes and High Speed Wind Streams* (Colorado Assoc. Univ. Press, Boulder, 1977)
T.H. Zurbuchen, Annu. Rev. Astron. Astrophys. **45**, 297 (2007)
T.H. Zurbuchen, S. Hefti, L.A. Fisk, G. Gloeckler, N.A. Schwadron, J. Geophys. Res. **105**, 18327 (2000)